

# Aerodynamic Noise Reduction Based on Bionic Blades with Non-Smooth Leading Edges and Curved Serrated Trailing Edges

W. Feng, K. Chen <sup>†</sup>, H. Gui, P. Zhao, R. Gao, and Y. Li

*College of Mechanical Engineering, Xinjiang University, Urumqi, Xinjiang, 830000, China*

<sup>†</sup>Corresponding Author Email: [chenkun\\_34@163.com](mailto:chenkun_34@163.com)

(Received November 14, 2022 accepted March 4, 2023)

## ABSTRACT

The flight of the owl is silent owing to non-smooth leading edges of the owl's wings and the curved serration of the feathers. This study applied this concept of bionics to blade design for horizontal axis wind turbines to reduce aerodynamic noise. The flow and sound field distribution around a rotating wind turbine with three blades were investigated. A numerical simulation method that combines large eddy simulation (LES) and FW-H acoustic equation was adopted to compare aerodynamic noise between the blade prototype and the bionic blade. The comparison revealed that the sound pressure level of the bionic blade was reduced over middle and high frequencies, thereby achieving a noise reduction of 6.9 dB. The intensity of the wake vortex shedding of the bionic blade was lower, and the interaction between the shedding vortices in the bionic blade was smaller compared with that in the prototype blade, indicating that the aerodynamic noise induced by the shedding vortex was effectively reduced.

**Keywords:** Wind turbine; Bionic design; CFD analysis; Aerodynamic noise; Noise mechanism.

## NOMENCLATURE

A	amplitude	N	number of sampling steps
$c$	chord length	$p$	convergence order
$C_p$	power coefficient	$r$	grid refinement rate
$d$	serration spacing	$S_b$	blade area
$D$	wind turbine diameter	$S_w$	owl wing area
$h$	serration height	$T$	thrust
$L$	blade length	$w$	serration width
$M$	torque	$\lambda$	wavelength
$n$	rotation speed		

## 1. INTRODUCTION

Wind energy is extensively used as a clean energy source to promote advancements in the wind power industry. However, environmental noise pollution caused by wind power equipment has become more prominent, especially because of aerodynamic noise generated by large-scale wind turbine structures with high tip speed ratios.

To reduce aerodynamic noise, studies have proposed design modifications, such as leading-edge protrusion and trailing-edge serration. A leading-edge protrusion is effective for controlling fluid flow on the top surface of the wing, according to theory (Mathews and Peake 2018; Lacagnina *et*

*al.* 2021), numerical simulation (Tong *et al.* 2018; Wang *et al.* 2019; Rao and Liu 2020), and experiments (Auris and Chong 2018; Teruaki *et al.* 2018; Chen *et al.* 2021b; Muthuramalingam *et al.* 2021). It can transform laminar flow into turbulent flow to stabilize the flow on the suction side, thereby delaying the vortex shedding caused by laminar separation and achieving noise suppression (Rao and Liu 2018). Howe (1991, 1998) used theoretical predictions to study the effect of sawtooth on the trailing edge scattering. Chong and Vathylakis (2015) experimentally investigated broadband noise at the edge of the tail of a plate. The vortex structure developed along the edges and exhibited strong three-dimensional properties. Further measurements and calculations performed by Velden *et al.* (2016) on the flow feature of an

airfoil plate at the trailing-edge of serration revealed that turbulent flow also tends to cause fluid to flow into gaps between serrations. This causes flow distortion and reduces the offsetting effect of turbulent convection at the edge, thereby decreasing the noise reduction potential of serration. Accordingly, *Avallone et al. (2017)* designed an iron-shaped sawtooth and analyzed its flow field in comparison with the conventional triangular trailing-edge sawtooth. The results indicated that the iron-shaped sawtooth shape reduced a broadband noise of 2 dB compared with a conventional sawtooth with a Strouhal number of less than 15. The greater noise reduction was attributed to scattered noise mitigation at the root edges of the serrations. These studies revealed that turbulence on the trailing-edge serrations can generate flow motion between the serration centerline and the edge, thereby affecting the noise reduction potential.

Several studies have focused on noise reduction using leading or trailing-edges in a single structure. In addition, the effects of multiple structures on airfoil noise have attracted considerable research attention, especially with the application of biological multi-featured structures. *Wang et al. (2017)* proposed a wavy leading edge bionic airfoil. The bionic structure was applied to convert the shedding vortices into conventional horseshoe-shaped vortices. *Wang et al. (2021)* adapted the owl wing ridge structure to airfoils with serrated leading edge for noise reduction. The results indicated that the bionic structure causes changes in the flow vortices such that the flow vortices separate into smaller horseshoe-shaped vortices; this was consistent with the findings of *Wang et al. (2017)*.

Thus far, most studies have focused on flat airfoils, but few studies have applied bionic structures to three-dimensional rotating blades for noise reduction. In this study, the effects of bionic structures on blade rotation were further investigated. Therefore, this study applied the non-smooth leading edge of owl wings and the curved serrated structure of feathers to the design of wind turbine blades. The aerodynamic noise of a three-dimensional rotating wind turbine blade was investigated to elucidate the effects of bionic structures on aerodynamic noise during rotation. Furthermore, the noise reduction mechanism during flow control was analyzed.

## 2. GEOMETRICAL MODELS

### 2.1 Prototype Blade

A scaled-down blade model with six types of airfoils of the NREL 5MW (*Jonkman et al. 2009*) wind turbine was used as a prototype blade. Fig. 1 illustrates the position of blades in different sections of the airfoil. Considering the time and the computation cost, the wind turbine was scaled according to principles of geometric and motion similarity. The scaling ratio was set to 50. According to the principle of motion similarity, the

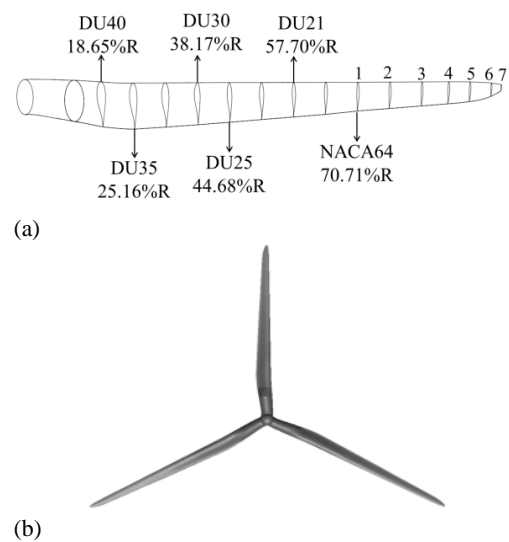


**Fig. 1. Prototype blade model of the NREL 5MW wind turbine with six types of airfoil in different section.**

tip speed ratio (TSR) of the blades should be set to similar values.

$$TSR = \frac{\pi n D}{60 u} \quad (1)$$

Where  $n$  denotes wind turbine rotation speed;  $u$  denotes rated wind speed;  $D$  denotes blade diameter.

The TSR values of the NREL turbine and the prototype were identical, as expressed in Eq. (2):

$$TSR_{NREL} = TSR_M \quad (2)$$

The prototype blade model is displayed in Fig. 1(b), and the similarity relationship for each parameter is illustrated in Table 1.

The parameters of the scaled-down prototype blade model are listed in Table 2.

**Table 1 Parameter similarity relationships**

Parameters	Relationships	Scale factor
Power ( $P$ )	$P_1/P_2=(R_1/R_2)^2$	$50^2$
Torque ( $M$ )	$M_1/M_2=(R_1/R_2)^3$	$50^3$
Thrust ( $T$ )	$T_1/T_2=(R_1/R_2)^2$	$50^2$
Length( $L$ )	$L_1/L_2=R_1/R_2$	50
Rotation speed ( $n$ )	$n_1/n_2=(R_1/R_2)^{-1}$	$50^{-1}$

**Table 2 Parameters of the scaled-down prototype wind turbine**

Parameters	NREL 5MW	Scaled-down model
Rated wind speed ( $m \cdot s^{-1}$ )	11.4	11.4
TSR	7	7
Power (W)	$5 \times 10^6$	2000
Wind turbine diameter (m)	126	2.52
Rotation speed ( $r \cdot min^{-1}$ )	12.1	605

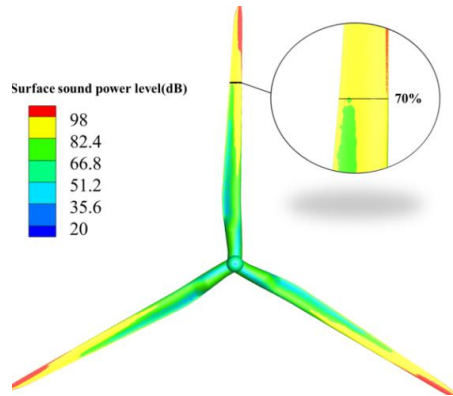


**Fig. 2. Distribution of sound power level on the blade surface.**

### 2.2 Bionic Blade

Aerodynamic performance should be maintained while reducing the aerodynamic noise of blades. To this end, the main distribution positions of the bionic structure should be determined. In this study, numerical simulations of the prototype blade were performed to determine the distribution of sound power levels. As illustrated in Fig. 2, the prototype blade exhibited a higher sound power within the range 70%–100% of the blade. Thus, the bionic structure was reconstructed at a position between 70% and 100% of the blade to achieve noise reduction.

The bionic non-smooth leading edge structure (Chen *et al.* 2021a) can be seen in Fig.3. The ratio of leading edge height to midline spacing of the wing is 0.12-0.19, while the ratio of leading edge height to chord length (c) is concentrated in 0.025-0.1 (Ren *et al.* 2008). So the parameters of the leading edge are amplitude (A) and wavelength ( $\lambda$ ). In this paper, we take  $A=0.025c$  and  $A/\lambda=0.125$ . The equation of such a leading edge profile is as follows:

$$y = \frac{A}{2} \cdot \sin\left(\frac{2\pi}{\lambda} \cdot x\right) \quad (3)$$

Table 3 shows the final design data. Since the blade positions 6–7 is too small, the tip section is designed separately by taking the average of the chord lengths of the adjacent airfoils at the blade tip.

**Table 3 Non-smooth leading edge geometry parameters**

Position	Chord length (c/mm)	Average chord length (c/mm)	Wavelength ( $\lambda$ /mm)	Amplitude (A/mm)	Governing equations
1	60.200	46.973	9.395	1.174	$y = -0.587 \times \sin\left(\frac{2\pi}{9.395} \times x\right)$
2	54.920				
3	50.360				
4	46.260				
5	41.720				
6	28.380	21.190	4.238	0.530	$y = -0.265 \times \sin\left(\frac{2\pi}{4.238} \times x\right)$
7	14.000				

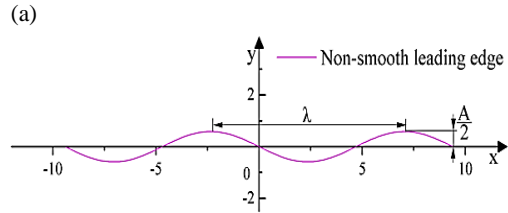
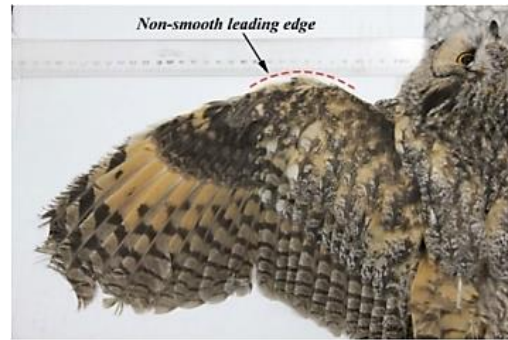


**Fig. 3. Outline of the leading edge, (a) The leading edge of an owl wing, (b) non-smooth leading edge structure.**

As illustrated in Fig. 4 (a), the serration in the owl's feather is curved. According to the data (Liao 2013) obtained for the owl serration structure, the curved serration structure was reconstructed on the blade based on the principle of geometric similarity. The scaling factor k is calculated as follows:

$$k = \sqrt{\frac{S_b}{S_w}} \quad (4)$$

Where  $S_b$  is the blade area and  $S_w$  is the owl wing area. Using the measured values of  $S_b$  and  $S_w$  in Table 4,  $k = 2$ . The curved trailing-edge serrations are illustrated in Fig. 4(b). The main parameters of the serrations are serration height (h), serration width (w), and serration spacing (d). Owl feather serrations have a root spacing of 0–1.12 mm. To prevent additional blunt trailing-edge noise and manufacturing problems, a spacing of  $d = 0.5$  mm was selected for serrations in the blade prototype designed in this study. This is a commonly used spacing size for trailing-edge serrations (Wang and Liu 2022). The final values of the curved serrations are listed in Table 4.

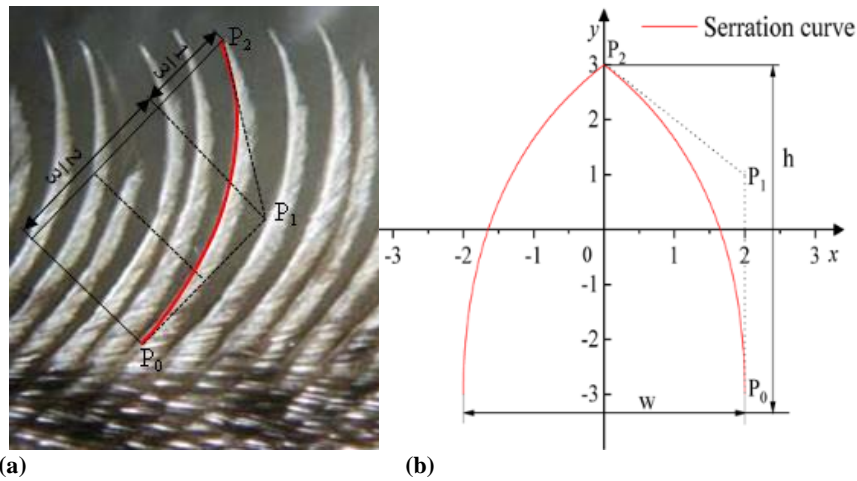


Fig. 4. Serrated structure, (a) serration structure of the feather, (b) serration on Bezier curve.

Table 4 Geometric values of wing and blade

Type	Area ( $S_w, S_b/\text{mm}^2$ )	Serration height (h/mm)	Serration width (w/mm)
Wing	30000	1.020–3.510	0.850–2.900
Blade	81800	2.040–7.020	1.700–5.800
Selected values	—	6	4
Selected value at the tip of the blade	—	3	2

The serration curve was fitted by the second-order Bezier curve  $B(t)$ . The  $B(t)$  is defined as follows:

$$B(t) = P_0(1-t)^2 + 2P_1t(1-t) + P_2t^2 \quad (5)$$

The equation was converted as follows:

$$B(t) = [P_0 \ P_1 \ P_2] \begin{bmatrix} 1 & -2 & 1 \\ 0 & 2 & -2 \\ 0 & 0 & 1 \end{bmatrix} \begin{bmatrix} 1 \\ t \\ t^2 \end{bmatrix} \quad (6)$$

Where  $P_0$  denotes the starting point coordinate,  $P_1$  denotes the curve shape control point coordinate,  $P_1 = 2/3 P_0P_2$ ,  $P_2$  denotes the end point coordinate.

The expressions for the curved serrations at blade positions 1–6 are as follows:

$$\begin{bmatrix} x(t) \\ y(t) \end{bmatrix} = \begin{bmatrix} -2t^2 + 2 \\ -2t^2 + 8t - 3 \end{bmatrix} \quad (7)$$

The size of the serrations of the trailing edge was designed separately for blade positions 6–7. With the ratio of serration height and width held constant, the serrations at blade positions 6–7 are expressed by Eq. (8). The blade serration dimensions are listed

in Table 4. The final two blades are depicted in Fig. 5.

$$\begin{bmatrix} x(t) \\ y(t) \end{bmatrix} = \begin{bmatrix} -t^2 + 1 \\ -t^2 + 4t - 1.5 \end{bmatrix} \quad (8)$$

### 3. METHODS

A commercially available CFD software (ANSYS-FLUENT) was used to simulate the flow and sound fields around the wind turbine. The numerical simulations presented in this paper were computed using a parallel PC with 64 GB RAM and a  $10 \times 3.2$  GHz CPU.

#### 3.1 Computational Domain and Grid

The influence of the tower on calculation results was neglected in simulations. The computational domain was divided into a rotational and a stationary domain. The rotating domain had a diameter of 1.1D and a width of 0.2D. The diameter of the stationary domain was 2.5D. The distance from the inlet to the rotating domain was 1.5D, and

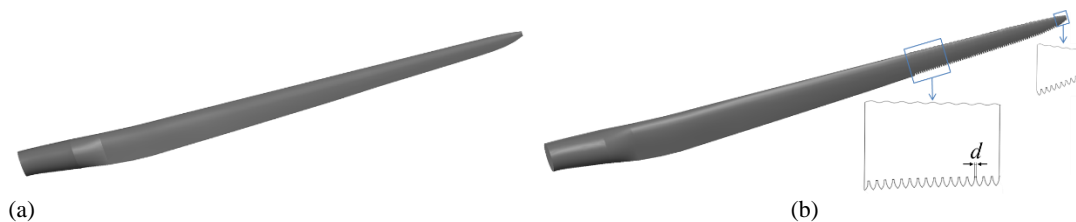


Fig. 5. Wind turbine blades, (a) prototype blade, (b) bionic blade.

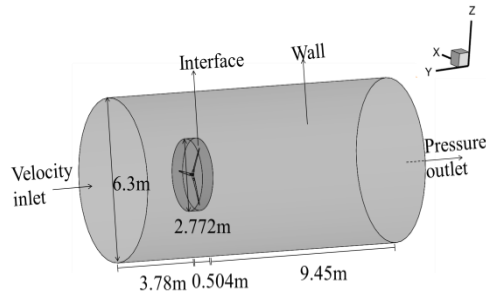


Fig. 6. Calculation domain.

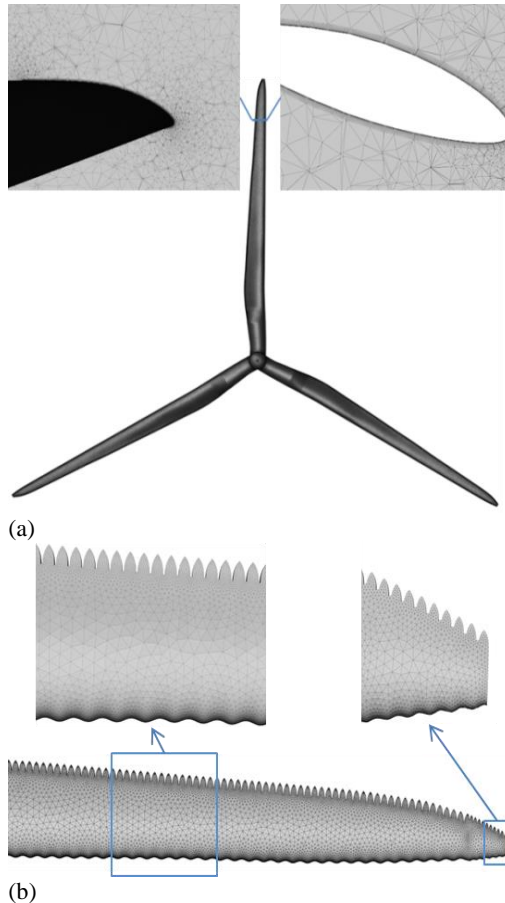


Fig. 7. Mesh distribution, (a) prototype blade surface mesh and nearby boundary layers, (b) bionic blade surface mesh.

the distance from the rotating domain to the outlet was  $3.75D$ . The rotational domain was connected by a cross interface and fixed as a slip grid to achieve blade rotation. The dimensions of the computational domain are illustrated in Fig. 6. The entire domain of numerical simulation was partitioned using an unstructured grid. The blade walls had boundary layers, and the height of the first layer was set to  $0.03\text{ mm}$  to realize a near-wall-grid ( $Y^+ < 1$ ) large eddy simulation (LES). A total of 10 structural mesh layers were created for the leading edge, the blade surface, and the curved serrated trailing edge, at a growth rate of 1.2. The blade surface grid and the nearby boundary layer are exhibited in Fig. 7.

### 3.2 Boundary Conditions

Air was selected as the fluid domain material. The simulation was performed under rated working conditions. The inlet was the velocity inlet with a rotation speed of 605 r/min and a wind speed of 11.4 m/s. The pressure outlet was the atmospheric pressure, and the blade wall was fixed as the no-slip wall.

The frequency range 0 to 20000 Hz was selected, and the time step of the sound field determined using Eq. (9) was  $2.5 \times 10^{-5}\text{ s}$ . The frequency resolution was set to 20 Hz, and the number of sampling steps ( $N$ ) was obtained using Eq. (10) as 2000 steps.

$$f_{max} = \frac{1}{2\Delta t} \quad (9)$$

Where  $f_{max}$  denotes the maximum frequency of 20,000 Hz and  $\Delta t$  denotes the time step.

$$N = \frac{1}{\Delta f \times \Delta t} \quad (10)$$

Where  $\Delta f$  denotes the frequency resolution.

### 3.3 Computational Models

To derive a non-constant field, the shear stress transport (SST)  $k-\omega$  model was applied to the steady-state flow field and LES combined with a wall-adapted local eddy-viscosity (WALE) subgrid scale model was applied to the transient state. The sound field around the monitoring site was calculated using the flow field results as the initial conditions for the Ffowcs Williams-Hawkins equation (FW-H equation). The sound field monitoring points are illustrated in Fig. 8. The SIMPLE consistent (SIMPLEC) algorithm was used for numerical simulations because SIMPLEC involves under-relaxation, which can accelerate convergence speed and save computation time. A least squares algorithm was used to obtain the gradients of the variables. Discrete momentum and transient equations were solved using a second-order implicit format with residuals set to  $10^{-4}$ .

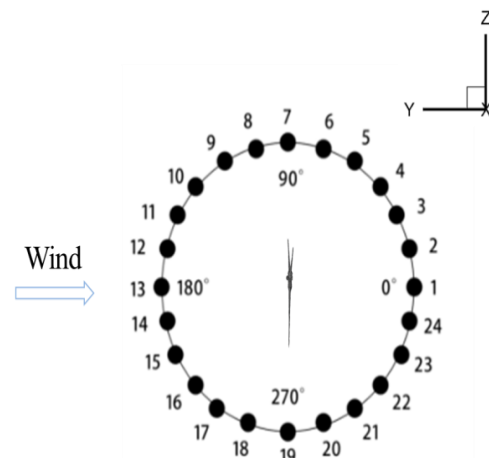


Fig. 8. Schematic of the distribution of sound monitoring points.

### SST k- $\omega$ model

The SST k- $\omega$  model (Menter 1994) can be used to determine the flow separation zone because it incorporates the advantages of both k- $\epsilon$  and k- $\omega$  models.

The turbulent kinetic energy k is expressed as follows:

$$\frac{\partial(\rho k)}{\partial t} + \frac{\partial(\rho k u_i)}{\partial x_i} = \frac{\partial}{\partial x_j} \left[ \left( \mu + \frac{\mu_t}{\sigma_k} \right) \frac{\partial k}{\partial x_j} \right] + \min(\mu_t S^2, 10\rho\beta^* k\omega) - \rho\beta^* f_{\beta^*} k\omega \quad (11)$$

The dissipation rate  $\omega$  is expressed as follows:

$$\frac{\partial(\rho k)}{\partial t} + \frac{\partial(\rho \omega u_i)}{\partial x_i} = \frac{\partial}{\partial x_j} \left[ \left( \mu + \frac{\mu_t}{\sigma_\omega} \right) \frac{\partial \omega}{\partial x_j} \right] + \frac{\alpha\rho}{\mu_t} \min(\mu_t S^2, 10\rho\beta^* k\omega) - \rho\beta^* f_{\beta^*} k\omega^2 + D_\omega \quad (12)$$

### LES Model

The LES method is used to simulate large eddies with the Navier-Stokes (N-S) equation, whereas the WALE subgrid scale model (Nicoud and Ducros 1999) is used to simulate small-scale eddies.

$$\frac{\partial \bar{u}_i}{\partial t} + \frac{\partial \bar{u}_i \bar{u}_j}{\partial x_j} = -\frac{1}{\rho} \frac{\partial \bar{p}}{\partial x_i} + \frac{\partial}{\partial x_j} \left( \nu \frac{\partial \bar{u}_i}{\partial x_j} \right) + \frac{\partial \tau_{ij}}{\partial x_j} \quad (13)$$

$$\frac{\partial \bar{u}_i}{\partial x_i} = 0 \quad (14)$$

### FW-H Equation

Ffowcs Williams and Hawkins (Ffowcs Williams and Hawkins 1969) considered moving wall factors, based on Lighthill's acoustic theory (Lighthill 1954), to the sound generation problem of fluids with arbitrary moving wall boundaries. The FW-H equation is expressed as follows:

$$\left( \frac{1}{c^2} \frac{\partial^2}{\partial t^2} - \frac{\partial^2}{\partial x_i^2} \right) p'(x_i, t) = \frac{\partial}{\partial t} \{ [\rho_0 v_n + \rho(u_n - v_n)] \delta(f) \} + \frac{\partial^2}{\partial x_i \partial y_i} [T_{ij} H(f)] - \frac{\partial}{\partial x_i} \{ [-p_{ij}' n_{ij} + \rho u_i (u_n - v_n)] \delta(f) \} \quad (15)$$

$$H(f) = \begin{cases} 0, & f(x_i, t) < 0 \\ 1, & f(x_i, t) \geq 0 \end{cases} \quad (16)$$

$$\delta(f) = \frac{\partial H(f)}{\partial f} \quad (17)$$

Where  $\frac{1}{c^2} \frac{\partial^2}{\partial t^2} - \frac{\partial^2}{\partial x_i^2}$  denotes the wave operator,  $p'(x_i, t)$  denotes the sound pressure.

### 3.4 Grid Independent Test

To quantify the grid discretization error, the grid convergence index (GCI) (Roache 1998) was calculated. Three grid sizes were used (see Table 5), with the power coefficient ( $C_P$ ) of each size selected

**Table 5 Variables employed in the Richardson extrapolation method**

Variable	Value
$N_1, N_2, N_3$	13.35, 7.85, 4.60 ( $\times 10^6$ )
$r_{21}$	1.3028
$r_{32}$	1.3254
$\Phi_1, \Phi_2, \Phi_3$	0.422, 0.417, 0.402
P	3.77
$\Phi_{\text{ext}}^{21}$	0.4249
$e_{\text{a}}^{21}$	1.18%
$e_{\text{ext}}^{21}$	0.68%
$\text{GCI}_{\text{fine}}^{21}$	0.86%

as the grid independence reference value (i.e.  $\Phi = C_P$ ).

$$C_P = \frac{2\pi nM}{0.5\rho\pi(D/2)^2 u^3} \quad (18)$$

Where  $M$  denotes the torque, and  $\rho$  denotes the fluid density.

Based on the values in Table 5, GCI is calculated as follows:

$$\text{GCI}_{\text{fine}}^{21} = \frac{1.25e_{\text{a}}^{21}}{(r_{21}^p - 1)} \quad (19)$$

Where  $e_{\text{a}}^{21}$  denotes the approximate relative error ( $e_{\text{a}}^{21} = |\frac{\Phi_1 - \Phi_2}{\Phi_1}|$ ,  $r$  denotes grid refinement rate and  $p$  denotes convergence order). The order of convergence can be calculated as follows:

$$p = \frac{1}{\ln(r_{21})} |\ln|\epsilon_{32}/\epsilon_{21}| + q(p)| \quad (20a)$$

$$q(p) = \ln \left( \frac{r_{21}^p - s}{r_{32}^p - s} \right) \quad (20b)$$

$$s = 1 \times \text{sgn}(\epsilon_{32}/\epsilon_{21}) \quad (20c)$$

The extrapolation value was  $\Phi_{\text{ext}}^{21} = 0.4249$ , the relative error was  $e_{\text{ext}}^{21} = 0.68$ , and the fine GCI was  $\text{GCI}_{\text{fine}}^{21} = 0.86\%$ .

$$\Phi_{\text{ext}}^{21} = (r_{21}^p \Phi_1 - \Phi_2) / (r_{21}^p - 1) \quad (21)$$

$$e_{\text{ext}}^{21} = \left| \frac{\Phi_{\text{ext}}^{21} - \Phi_1}{\Phi_{\text{ext}}^{21}} \right| \quad (22)$$

The expected error band for grid  $N_1 = 13.35 \times 10^6$  was approximately 0.86%, which satisfies the grid requirements. Considering the complex structure of the bionic blade, the maximum mesh number of the bionic blade was approximately 15 million.

The prototype blade mesh  $N_1$  was numerically simulated. The obtained  $C_P$  and thrust values were compared with the reported values (Jonkman *et al.* 2009). The results indicated errors of 4.52% and 1.7% in the  $C_P$  and thrust values have, respectively, which were acceptable for the calculations. The accuracy of the mesh was further confirmed. The results are illustrated in Fig. 9.

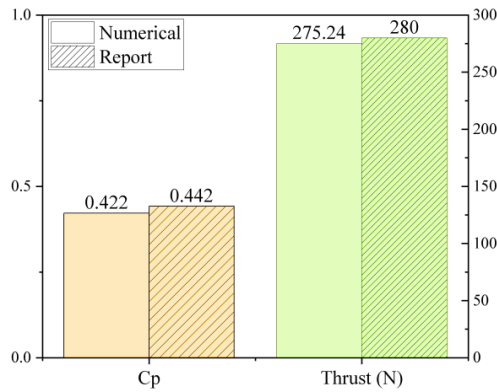


Fig. 9. Power coefficient and thrust values.

#### 4. RESULTS AND DISCUSSION

##### 4.1 Sound Source and Spectrum Analysis

Owing to the directionality of sound, noise propagates with different intensities in different directions.

To elucidate the influence of the bionic structure on the sound directivity of the wind turbine, the sound pressure levels (SPLs) were measured at some monitoring points around the wind turbine. Fig. 10 illustrates the sound directional distribution of the two blades. The overall trend of sound directivity distribution is identical for the two kinds of blades, indicating that the bionic structure did not change the sound directivity of the blade. Therefore, the SPL of bionic blade was lower compared with that of the prototype blade at all azimuth angles. The SPL reduction was most notable (6.9 and 5.6dB) at 90° and 270° azimuth angles.

Sound pressure spectrograms indicated changes in the SPL over different frequency ranges. Fig. 11 displays the spectrograms of the two blades at the monitoring point of 90° azimuth, where the SPL peak frequencies of the two blades were similar and appeared at 1600 Hz. According to the overall sound frequency spectrum, the influence of the bionic blade on the SPL was mostly concentrated in middle and high frequency regions. Comparing the results of the spectrum simulation analysis revealed that the influence of the bionic blade on the SPL was primarily concentrated in the mid- and high-frequency regions. To comprehensively analyze the

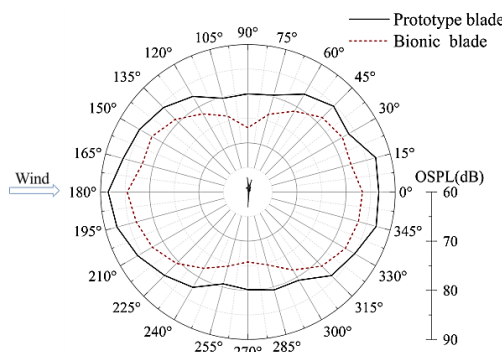


Fig. 10. Sound directivity distribution.

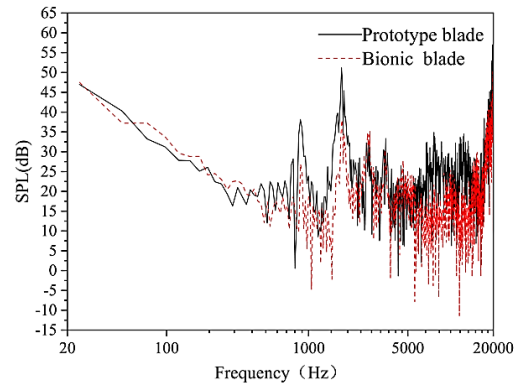


Fig. 11. Spectrograms of SPLs for two blades.

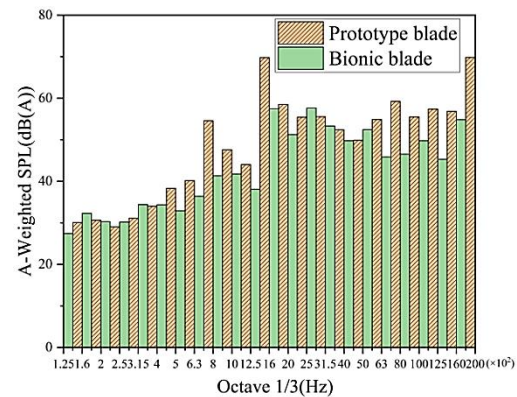


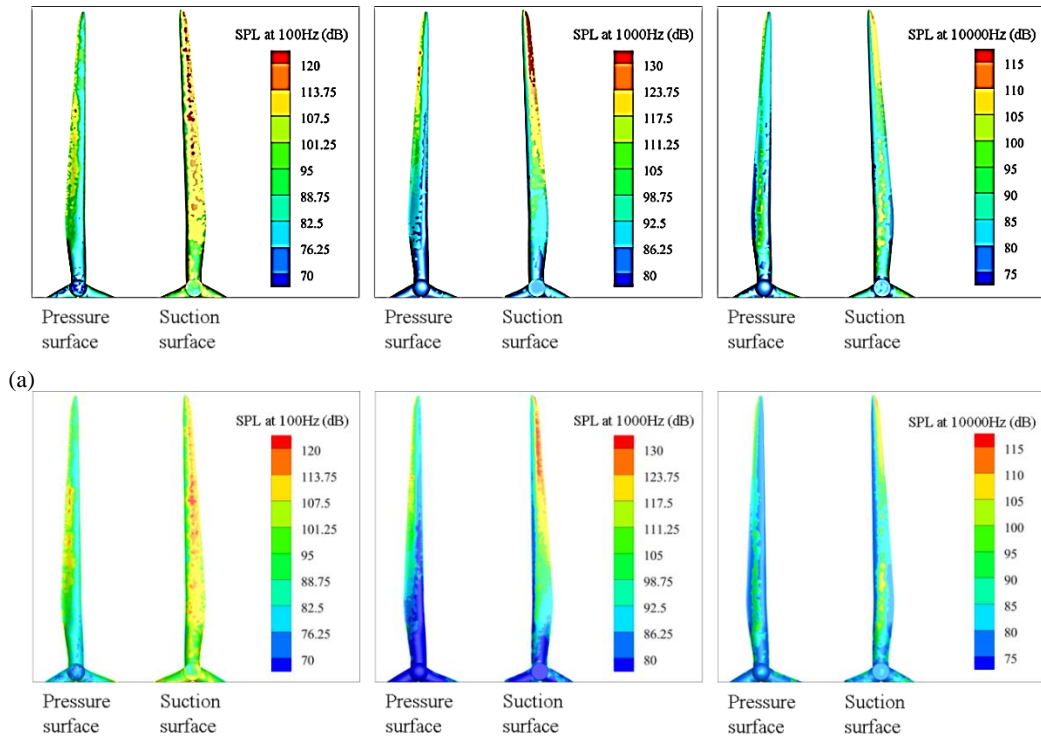
Fig. 12. One-third octave band noises of the two blades.

SPL distribution of the wind turbine blade over each frequency range, A-weighted SPL distributions over the one-third octave were obtained, as illustrated in Fig. 12. The noise was primarily generated over the mid- and high-frequency bands, and the SPL of both blades exhibited identical variation trends. Comparing the A-weighted SPL distributions of the two blades revealed that the bionic blade significantly reduced the peak frequency at 1600 Hz. In addition, the bionic blade exhibited a notable noise reduction effect between 6300 and 20000 Hz. The bionic blade's noise reduction frequency was primarily concentrated on the mid- and high-frequency regions. Over the main noise generation frequency band, the bionic blade exhibited better noise reduction performance.

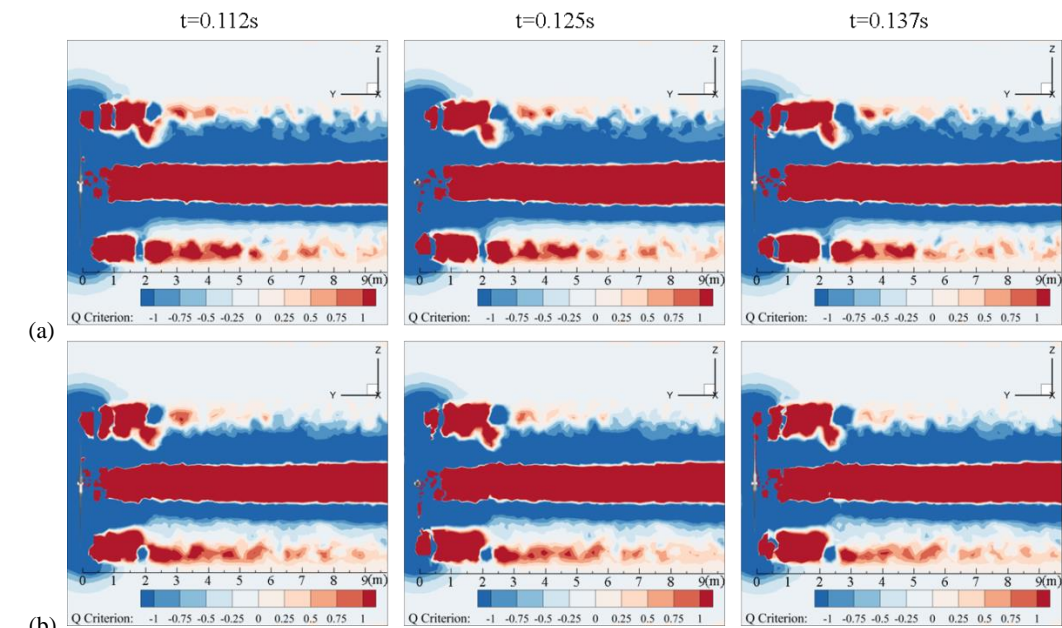
##### 4.2 Sound Pressure Contours

Fig. 13 displays the sound pressure contours of the two blades at different frequencies under rated operating conditions. Figs. 13(a) and (b) illustrate the corresponding contours of the prototype and the bionic blade, respectively, at center frequencies of 100 Hz, 1,000 Hz, and 10,000 Hz. The location of the high sound pressure region varied with frequency. As illustrated in Figs. 13(a) and (b), the high sound pressure region was primarily distributed on the suction surface.

Comparison between the prototype and bionic blades revealed that the high sound pressure area with a center frequency of 100 Hz in the low-



**Fig. 13.** Sound pressure contours on the blade surface, (a) prototype blade, (b) bionic blade.



**Fig. 14.** Vorticity distribution of the blade in the  $x = 0$  m plane, (a) prototype blade, (b) bionic blade.

frequency band was distributed on the entire blade. Because the bionic structure was applied only to 70% to 100% of the blade's position, the effect of the bionic structure was not substantial over the low-frequency band. Even in middle part of the blade, the area of the high sound pressure region on the pressure surface increased. In the contour plots for the center frequencies of 1000 Hz and 10,000 Hz, the high sound pressure distribution areas of the bionic blade in the suction and pressure surfaces were narrower. This was because the bionic

structure affected the surface sound pressure distribution, thus reducing aerodynamic noise from the blades.

### 4.3 Vortex Distribution

The coherent distribution of the vortex shedding structure dominated the mechanism of noise generation and propagation. Figure 14 illustrates the vortex distribution of the prototype and bionic

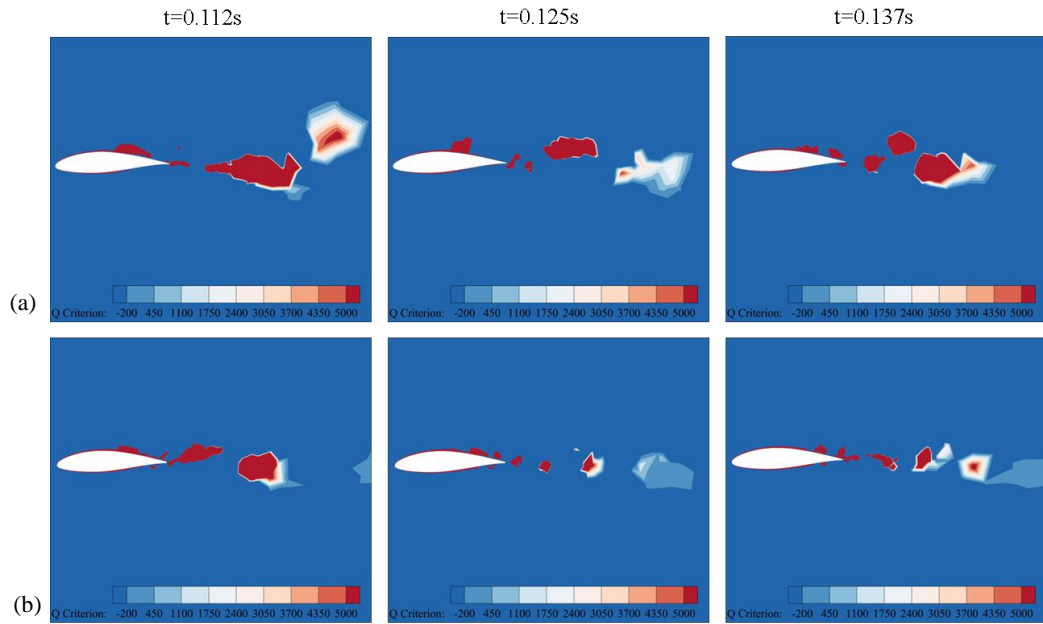


**Fig. 15. Vortex distribution at 80% of the blade cross-section, (a) prototype blade, (b) bionic blade.**

blades at various times. The Q criterion of the LES model may be used to describe the vortex distribution. The Q criterion can be expressed as follows:

$$Q = \frac{1}{2} (\Omega_{ij}\Omega_{ij} - S_{ij}S_{ij}) \quad (23)$$

Where the vortex  $\Omega_{ij} = \frac{1}{2} \left( \frac{\partial u_i}{\partial x_j} - \frac{\partial u_j}{\partial x_i} \right)$ , strain rate tensor  $S_{ij} = \frac{1}{2} \left( \frac{\partial u_i}{\partial x_j} + \frac{\partial u_j}{\partial x_i} \right)$ , and the Q value distinguishes between different areas. A higher positive Q value indicates a region of high vorticity and vice versa.

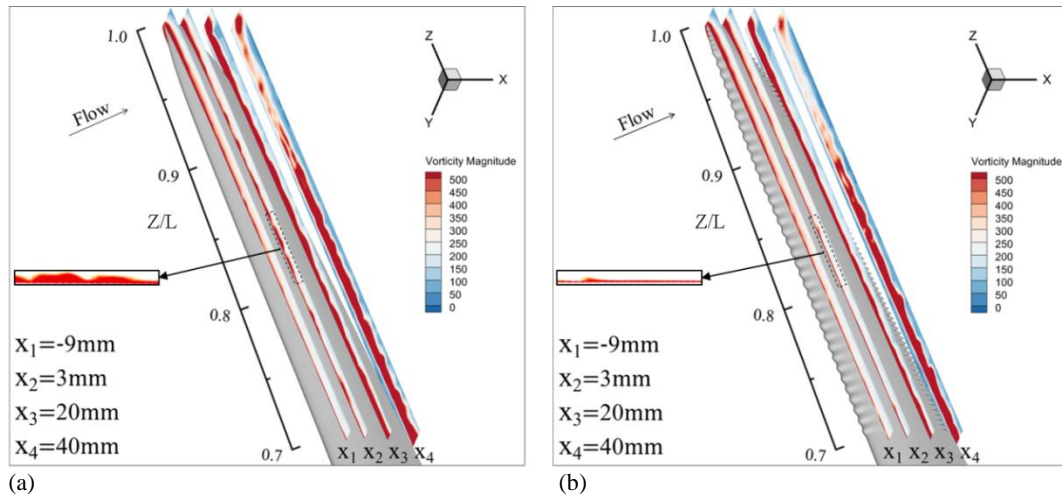
According to the calculated values of the Q criterion, the vortex shedding is concentrated in the blade tip area. The process of vortex shedding was observed at different times. From  $t = 0.112$  to  $0.137$ s for the two kinds of blades, the vortices at the blade tip in the vortex shedding region gradually separated and evolved into smaller vortices, whereas the vortex intensity gradually decreased and finally dissipated. In the vortex distribution at the blade tip region, the wake shedding vortex structure of the prototype blade was larger, whereas that of the bionic blade was smaller and more elongated. During vortex dissipation, the vortex dissipation in the vortex shedding area of the bionic blade was faster. The bionic structure prevented the creation of large-scale vortices while transforming the vortex system into a small-scale vortex system, which increased the dissipation rate. During the dissipation of large-scale vortex structure into small-scale vortex structures, some energy was depleted continuously, which in turn reduces noise generation.

Figure 15 illustrates the vortex volume distribution at 80% cross-section of the two kinds of blades. The vortex volume was primarily concentrated at the blade suction surface, whereas the vortex separated

and shed when approaching the trailing edge. Comparison revealed that the vortex separation point of the bionic blade was more backward. This can be attributed to the special leading-edge structure that stabilized the suction side flow and thus effectively delayed vortex separation, thus decreasing the overall size of the vortex structure. In addition, the periodic large scale vortex was suppressed by the serrated trailing edge of the bionic blade. Finally, the large-scale vortex structure transformed into a finer vortex structure. Larger vortex spacing between the shedding vortices of the bionic blade was also observed. The larger spacing reduced the interaction between the shedding vortices, resulting in faster dissipation of the vortices and noise reduction in bionic blades.

The vortex volume is primarily generated on suction surface. The vorticity distributions in different unfolded sections of the blade suction surface were statistically determined over the time period from  $0.112$  to  $0.137$  s. Fig. 16 displays the vorticity distribution of the four cross sections arranged in the order  $x_1$ ,  $x_2$ ,  $x_3$ , and  $x_4$  from the leading edge to the trailing edge.

The vorticity was primarily distributed near the blade wall because of the shear effect of the boundary layer between the fluid above and below the blade attachment layer, resulting in small-scale turbulence. As illustrated in Fig.16, the vortex separation area between the suction surfaces of the two blades grew increasingly along the spreading direction. The disturbance of the vortex volume of the prototype blade began at  $x_2 = 3$  mm section, and a large region of disturbance was formed at  $x_3 = 20$  mm. The disturbance of the vortex volume of the bionic blade started only at the cross-section at  $x_3 = 20$  mm. This can be attributed to the leading-edge structure, which improved the spreading correlation of the fluid, thereby allowing it to flow faster to the



**Fig. 16. Distribution of time-averaged vorticity in the blade spreading direction, (a) Prototype blade, (b) Bionic blade.**

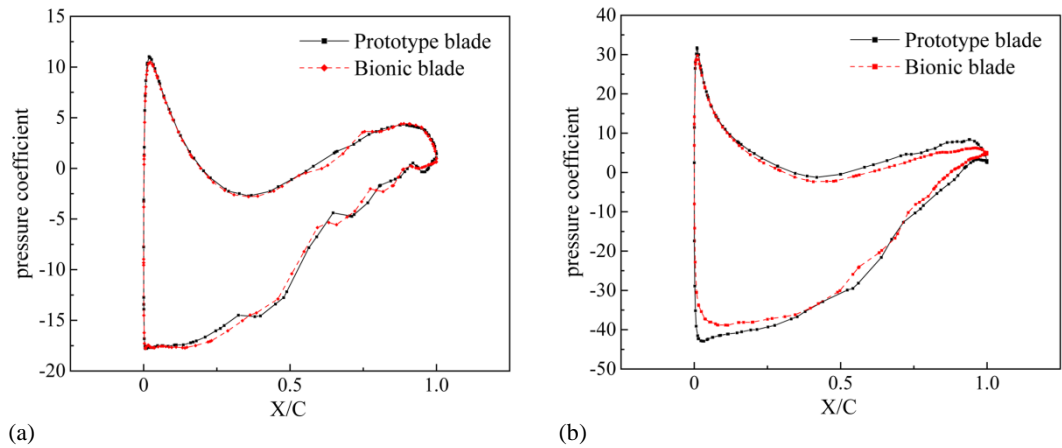


**Fig. 17. Pressure coefficients, (a) 45% cross-section, (b) 80% cross-section.**

trailing edge. At the cross-section at  $x_4 = 40$  mm, the intensity of vortex shedding at the trailing edge of the bionic blade was considerably lower than that of the prototype blade. This result is consistent with that illustrated in Fig. 15.

The bionic blade interfered with the formation of large vortex clusters because of the serration, thereby increasing the frequency of vortex shedding, accelerating the dissipation of the vortex cluster, and reducing the intensity of vortex shedding. Therefore, the aerodynamic noise related to vortex shedding was reduced.

#### 4.4 Aerodynamic performance

Figure 17 displays the pressure coefficient distribution at 45% (ungeometrically modified section) and 80% (geometrically modified section) of the blade spreading section. The surface pressure coefficient distribution in both blades at the 45% section was identical, and the overall pressure difference of the blade surface at the 80% section of the bionic blade was smaller. This indicated that the bionic blade at the 45% cross-section maintained the blade surface flow, and the bionic structure had less influence on the blade surface flow in the

ungeometrically modified section. The bionic blade at the 80% cross section influenced the blade surface pressure difference, but the overall power coefficient  $C_P = 0.413$ , compared to the prototype blade  $C_P = 0.422$ , the power coefficient reduction rate was 2.13%, indicating that the aerodynamic performance of the bionic blade did not deteriorate substantially (Oerlemans *et al.* 2001). Considering the main contribution of the bionic blade to aeroacoustics, the reduction of the aerodynamic performance over a certain range is acceptable.

### 5. CONCLUSIONS

In the present study, bionic blades with non-smooth leading edge and curved serrated trailing edge were designed based on the owl wing and feather structure features. The sound field characteristics of both blades were compared and analyzed through numerical simulations under the same operating conditions. Furthermore, the effects of the bionic structure on the flow field distribution of the blades were discussed. The main conclusions of the work are as follows.

When comparing the two blades, the bionic blade reduced the SPL distribution over middle and high frequencies.

The bionic structure did not affect the trend of the sound direction distribution. Moreover, when comparing the two blades, the bionic blade reduced sound distribution in all directions. The overall SPL was reduced by a maximum of 6.9 dB, and the noise reduction rate was 8.63%.

The bionic structure primarily affected the sound pressure distribution on the suction surface of the blade. At frequencies between 1,000 Hz and 10,000 Hz, the area of high sound pressure distribution on the suction surface of the bionic blade was smaller.

The vortex separation position of the non-smooth leading edge on the surface of the bionic blade changes to a position closer to the trailing edge.

The curved serration converts large-scale vortices into small-scale vortices and accelerates the dissipation of the trailing edge vortex population, which effectively reduces the aerodynamic noise associated with the shedding vortex.

The reduction of the aerodynamic performance of the bionic blades within a certain range is acceptable. The overall power coefficient was reduced by 2.13% compared with that of the prototype blade.

#### ACKNOWLEDGEMENTS

This study was funded by the National Natural Science Foundation of China (No. 51765062); the Natural Science Foundation of Xinjiang Uygur Autonomous Region, China (No. 2022D01C33); the Graduate Research Innovation Project of Xinjiang Uygur Autonomous Region, China (No. XJ2022G049); and the National Innovation Training Program for college students, China (No. 202210755123).

#### REFERENCES

- Auris, J. and T. P. Chong (2018). On the leading edge noise and aerodynamics of thin aerofoil subjected to the straight and curved serrations. *Journal of Sound and Vibration* 425, 324-343.
- Avallone, W. C. P. Velden and D. Ragni (2017). Benefits of curved serrations on broadband trailing-edge noise reduction. *Journal of Sound and Vibration* 400, 167-177.
- Chen, K., W. Yao, J. Wei, R. Gao and Y. Li (2021a). Bionic coupling design and aerodynamic analysis of horizontal axis wind turbine blades. *Energy Science & Engineering* 9, 1826-1838.
- Chen, W., W. Qiao, W. Duan and Z. Wei (2021b). Experimental study of airfoil instability noise with wavy leading edges. *Applied Acoustics* 172, 107671.
- Chong, T. and A. Vathylakis (2015). On the aeroacoustic and flow structures developed on a flat plate with a serrated sawtooth trailing edge. *Journal of Sound & Vibration* 354(10), 65-90.
- Ffowcs Williams, J. E. and D. L. Hawkings (1969). Sound generation by turbulence and surfaces in arbitrary motion. *Philosophical Transactions of the Royal Society of London. Series A, Mathematical and Physical Sciences* 264, 321-342.
- Howe, M. S. (1991). Aerodynamic noise of a serrated trailing edge. *Journal of Fluids and Structures* 5(1), 33-45.
- Howe, M. S. (1998). Noise produced by a sawtooth trailing edge. *Acoustical Society of America Journal* 90(1), 482-487.
- Jonkman, J., S. Butterfield, W. Musial and G. Scott, (2009). *Definition of A 5-MW Reference Wind Turbine for Offshore System Development*. National Renewable Energy Laboratory (NREL)
- Lacagnina, G., P. Chaitanya and J. H. Kim (2021). Leading edge serrations for the reduction of aerofoil self-noise at low angle of attack, pre-stall and post-stall conditions. *International Journal of Aeroacoustics* 20(1), 130-156.
- Liao, G. (2013) *Aerodynamic and Acoustic Properties of Long-Eared Owl Wings and Their Bionic Applications*. Ph. D. thesis, the Jilin University, Ji Lin, china.
- Lighthill, M. J. (1954). On sound generated aerodynamically II. Turbulence as a source of sound. *Proceedings of the Royal Society of London. Series A*, 222, 1-32.
- Mathews, J. R. and N. Peake (2018). An analytically-based method for predicting the noise generated by the interaction between turbulence and a serrated leading edge. *Journal of Sound and Vibration* 422, 506-525.
- Menter, F. (1994). Two-equation eddy-viscosity turbulence models for engineering applications. *AIAA Journal* 32(08), 1598-605.
- Muthuramalingam, M., E. Talboys, H. Wagner and C. Bruecker (2021). Flow turning effect and laminar control by the 3D curvature of leading edge serrations from owl wing. *Bioinspiration & Biomimetics* 16(2), 026010.
- Nicoud, F. and F. Ducros (1999). Subgrid-scale stress modelling based on the square of the velocity gradient tensor. *Flow, Turbulence and Combustion* 62, 183-200.
- Oerlemans, S., J. Schepers, G. Guidati and S. Wagner (2001). Experimental demonstration of wind turbine noise reduction through optimized airfoil shape and trailing-edge serrations. In *Proceedings of the European Wind Energy Conference*.
- Rao, C. and H. Liu (2018) Aerodynamic robustness in owl-inspired leading-edge serrations: a computational wind-gust model. *Bioinspiration & Biomimetics* 13(5), 056002.
- Rao, C. and H. Liu (2020). Effects of reynolds number and distribution on passive flow

- control in owl-inspired leading-edge serrations. *Integrative and Comparative Biology* 60(5), 1135-1146.
- Ren, L., S. Sun and C. Xu (2008). Anechoic noise reduction mechanism of the non-smooth form of the leading edge of the owl wing. *Journal of Jilin University* 38,126-131.
- Roache, P. J. (1998). Verification and Validation in Computational Sciencend *Engineering, Computing in Science Engineering*, 8-9
- Teruaki, I., U. Tetsuya and N. Toshiyuki (2018). Morphology effects of leading-edge serrations on aerodynamic force production: an integrated study using piv and force measurements. *Journal of Bionic Engineering* 15(4), 661-672.
- Tong, F., W. Qiao, W. Chen, H. Chen, R. Wei and X. Wang (2018). Numerical analysis of broadband noise reduction with wavy leading edge [J]. *Chinese Journal of Aeronautics* 31(7), 1489-1505.
- Velden, W. C. P., A. H. Van Zuijlen and D. Ragni (2016). Flow topology and noise emission around straight, serrated and slitted trailing edges using the lattice Boltzmann methodology. In *22nd AIAA/CEAS Aeroacoustics Conference American Institute of Aeronautics and Astronautics Inc.*
- Wang, B., J. Liu and Q. Li, (2019). Numerical studies of reverse flows controlled by undulating leading edge. *Science China Physics, Mechanics & Astronomy* 62, 974712.
- Wang, J., C. Zhang and Z. Wu (2017). Numerical study on reduction of aerodynamic noise around an airfoil with biomimetic structures. *Journal of Sound and Vibration* 394, 46-58.
- Wang, L. and X. Liu (2022). Aeroacoustic investigation of asymmetric oblique trailing-edge serrations enlightened by owl wings. *Physics of Fluids* 34, 015113.
- Wang, L., X. Liu and D. Li (2021). Noise reduction mechanism of airfoils with leading-edge serrations and surface ridges inspired by owl wings. *Physics of Fluids* 33(1), 015123.